Advanced High-Voltage All-Solid-State Li-Ion Batteries Enabled by a Dual-Halogen Solid Electrolyte

Shumin Zhang, Feipeng Zhao, Shuo Wang, Jianwen Liang, Jian Wang, Changhong Wang, Hao Zhang, Keegan Adair, Weihan Li, Minsi Li, Hui Duan, Yang Zhao, Ruizhi Yu, Ruying Li, Huan Huang, Li Zhang, Shangqian Zhao, Shigang Lu, Tsun-Kong Sham,* Yifei Mo,* and Xueliang Sun*

Solid-state electrolytes (SEs) with high anodic (oxidation) stability are essential for achieving all-solid-state Li-ion batteries (ASSLIBs) operating at high voltages. Until now, halide-based SEs have been one of the most promising candidates due to their compatibility with cathodes and high ionic conductivity. However, the developed chloride and bromide SEs still show limited electrochemical stability that is inadequate for ultrahigh voltage operations. Herein, this challenge is addressed by designing a dual-halogen Li-ion conductor: $Li_3InCl_{4.8}F_{1.2}$. F is demonstrated to selectively occupy a specific lattice site in a solid superionic conductor (Li_3InCl_6) to form a new dual-halogen solid electrolyte (DHSE). With the incorporation of F, the $Li_3InCl_{4.8}F_{1.2}$ DHSE becomes dense and maintains a room-temperature ionic conductivity over 10^{-4} S cm^{-1}. Moreover, the $Li_3InCl_{4.8}F_{1.2}$ DHSE exhibits a practical anodic limit over 6 V (vs Li/Li$^+$), which can enable high-voltage ASSLIBs with decent cycling. Spectroscopic, computational, and electrochemical characterizations are combined to identify a rich F-containing passivating cathode-electrolyte interface (CEI) generated in situ, thus expanding the electrochemical window of $Li_3InCl_{4.8}F_{1.2}$ DHSE and preventing the detrimental interfacial reactions at the cathode. This work provides a new design strategy for the fast Li-ion conductors with high oxidation stability and shows great potential to high-voltage ASSLIBs.

1. Introduction

All-solid-state Li-ion batteries (ASSLIBs) have been of significant interest due to the use of solid-state electrolytes (SEs) which replace the conventional flammable liquid electrolytes and possess improved safety.[1] Many SEs are predicted to be excellent for high-voltage applications where conventional liquid electrolytes decompose.[2] In the early stages of development, several sulfide compounds[3] were reported to possess high ionic conductivity that is comparable to those of conventional liquid electrolytes. Nevertheless, it is still challenging for them to be used directly in commercialized batteries due to the compatibility issues between SEs and electrode materials, air sensitivity (H_2S generation), as well as their limited electrochemical windows.[4] Recently, apart from the sulfide SEs with divalent anions, halide SEs have emerged as attractive alternatives due to the monovalent halogen anions having

S. Zhang, F. Zhao, Dr. J. Liang, Dr. C. Wang, K. Adair, Dr. W. Li, M. Li, Dr. H. Duan, Dr. Y. Zhao, Dr. R. Yu, R. Li, Prof. X. Sun
Department of Mechanical and Materials Engineering
University of Western Ontario
London, Ontario N6A 5B9, Canada
E-mail: xsun9@uwo.ca

S. Zhang, Dr. W. Li, M. Li, Prof. T. K. Sham
Department of Chemistry
University of Western Ontario
London, Ontario N6A 5B7, Canada
E-mail: tsham@uwo.ca

Dr. S. Wang, Prof. Y. Mo
Department of Materials Science and Engineering
University of Maryland
College Park, MD 20742, USA
E-mail: yfmo@umd.edu

Dr. J. Wang
Canadian Light Source Inc.
University of Saskatchewan
Saskatoon, Saskatchewan S7N 2V3, Canada

Dr. C. Wang, Dr. H. Huang
Glabat Solid-State Battery Inc.
700 Collip Circle, London, ON N6G 4X8, Canada

Dr. H. Zhang
School of Metallurgical and Ecological Engineering
University of Science and Technology Beijing
30 Xueyuan Road, Haidian Distinct, Beijing P.C. 100083, China

Dr. L. Zhang, Dr. S. Zhao, Dr. S. Lu
China Automotive Battery Research Institute Co. Ltd
5th Floor, No. 43, Mining Building, North Sanhuan Middle Road, Haidian District, Beijing P.C. 100088, China

Coulombic interactions with Li ions, which facilitates Li-ion conduction.[5] The other advantage of halide materials is their high theoretical anodic limits, as exemplified by >4 V (vs Li/Li$^+$) for chloride compounds and over 6 V for fluoride compounds.[6] While fluoride SEs may have higher voltage stability, they have been shown to possess relatively lower Li-ion conductivity due to the strong electronegativity of fluorine.[7] Moreover, a series of advanced chloride SEs (Li$_3$InCl$_6$[5b,6a], Li$_3$ErCl$_6$,[8] Li-Sc-Cl[5c,d], etc.) have been reported not only possessing high ionic conductivity over 1 mS cm^{-1}, but also having excellent cathode compatibility to realize good battery performance without any additional protection coatings on the cathode materials.[9] The very recently developed Li$_{3-x}$Y$_{1-x}$Zr$_x$Cl$_6$[10] and Li$_{2+x}$Zr$_{1-x}$Fe$_x$Cl$_6$[11] using earth-abundant and low-cost elements make chloride SEs commercially important. Despite chloride SEs being able to support ASSLIBs cycling up to a cut-off voltage around 4.5 V, these compounds are still inadequate for LIBs operating at higher voltages. This downside originates from the oxidation of Cl$^-$ above 4.3 V in chloride SEs along with the formation of other Li-deficient metal-chloride products (ErCl$_3$, InCl$_3$, etc.), which lacks sufficient Li-ion conductive paths and continuously consumes SEs to deteriorate the performance of full cells.[12] Therefore, the problems associated with the SE/cathode interface should be solved for the development of high-voltage ASSLIBs.

Previous research for improving the compatibility of the SE/cathode interface has mainly relied on protective coatings.[13] In general, various artificial coatings are utilized to modify the cathode materials, which physically protect the SEs from oxidation by the electroactive cathode materials.[13a] A perfect coating layer featuring Li-ion conduction, electronic insulation, and (electro)chemical stability not only prolongs the cycle life of ASSLIBs at high applied potentials, but also acts as an additional SE to extend the anodic limit of the SE itself.[14] However, compared with the direct use of a well-rounded SE, the processing of additional artificial coatings adds complication, is time-consuming, and can be costly.[13] As such, it is highly desired to develop SEs which can adopt the additional benefits of artificial coatings.

Herein, we propose to design a novel SE to enable high-voltage ASSLIBs. The in situ generation of passivating interphases with favorable Li-ion diffusion pathways is expected to suppress the SEs degradation and continuous interfacial reactions. Guided by this, a dual-halogen solid electrolyte (DHSE) is demonstrated where fluorine (F) is employed to selectively occupy a specific lattice site (Cl-8j) in Li$_3$InCl$_6$ SE to form a new SE: Li$_3$InCl$_{4.8}$F$_{1.2}$. With the incorporation of F, the practical oxidation limit of DHSE is enhanced to over 6 V. Both experimental and computational results identify that the F-containing passivating interphases are generated in situ, contributing to the enhanced anodic (oxidation) stability of Li$_3$InCl$_{4.8}$F$_{1.2}$ and stabilization on the surface of cathodes at high cut-off voltages. As a proof of concept, this Li$_3$InCl$_{4.8}$F$_{1.2}$ DHSE is directly matched with bare high-voltage LiCoO$_2$ (LCO), enabling ASSLIBs to stably operate at room temperature (RT) at a cut-off voltage of 4.8 V (vs Li/Li$^+$). Scanning transmission X-ray microscope (STXM) combined with advanced ptychography technique visualizes an F-rich cathode-electrolyte interface (CEI), which is further analyzed by X-ray absorption spectroscopy (XAS) showing LiF is the major interfacial component. This work presents a SE design strategy exemplified through the Li$_3$InCl$_{4.8}$F$_{1.2}$ DHSE with high practical anodic stability derived from the formation of a fluorinated interface, opening up new opportunities for the ultrahigh-voltage ASSLIBs.

2. Results and Discussion

2.1. Synthesis and Characterizations of Li$_3$InCl$_{4.8}$F$_{1.2}$ DHSE

Li$_3$InCl$_{4.8}$F$_{1.2}$ DHSE was obtained via a two-step solid reaction method. The first ball milling step was employed to mix the precursors, which is accompanied by the formation of partially crystallized products. Subsequently, a post-annealing step at a relatively low temperature can improve crystallinity and ionic conductivity.[5b] Synchrotron X-ray diffraction (SXRD) ($\lambda = 0.729293$ Å) was used to study the phase composition of the products at different stages. As shown in **Figure 1**a-1, the diffraction peaks of the Li$_3$InCl$_{4.8}$F$_{1.2}$ DHSE obtained after annealing become obviously sharper than the ball milling sample (denoted as Li$_3$InCl$_{4.8}$F$_{1.2}$ BM), indicating improved crystallinity in the final product. Compared with the diffraction pattern of annealed Li$_3$InCl$_6$ without F incorporation, the peaks of Li$_3$InCl$_{4.8}$F$_{1.2}$ DHSE shift to a higher 2θ angle (see the magnified regions in Figure 1a-2,1a-3), but are still assigned to a monoclinic phase (ICSD No. 04-009-9027). This suggests that the lattice space of Li$_3$InCl$_{4.8}$F$_{1.2}$ DHSE becomes contracted due to the partial replacement of Cl by F with a smaller ionic radius (F$^-$: 133 pm < Cl$^-$: 181 pm). SEM images depict a pelletized Li$_3$InCl$_{4.8}$F$_{1.2}$ with dense and compact morphology from the top-view observation (Figure 1b-1 and Figure S1, Supporting Information). In sharp contrast, without the incorporation of F, the electrolyte particles are disconnected and there are several obvious cracks on the surface of the pelletized Li$_3$InCl$_6$ (Figure 1b-2). Such a morphological difference can also be verified in Figure S2, which depicts the porosity of Li$_3$InCl$_{4.8}$F$_{1.2}$ pellet is much lower than that of Li$_3$InCl$_6$ under various pressures. Therefore, Li$_3$InCl$_{4.8}$F$_{1.2}$ DHSE has an advantage over Li$_3$InCl$_6$ SE due to its intimate contact and confined effect with the cathode material.[15] The energy-dispersive X-ray spectroscopy (EDS) mapping of the Li$_3$InCl$_{4.8}$F$_{1.2}$ DHSE shows the most homogeneous dispersion of In, Cl, and F elements (Figure 1c), indicating the complete reaction of various precursors. The ionic conductivity of Li$_3$InCl$_{4.8}$F$_{1.2}$ DHSE is measured to be 5.1×10^{-4} S cm^{-1} at RT (Figure 1d), which is lower than that of the Li$_3$InCl$_6$ (1.3×10^{-3} S cm^{-1}), coordinating with their Li-ion diffusivity trend from AIMD simulations[16] (Figure S3, Supporting Information). The Li-ion diffusion mechanism of the lower conductive Li$_3$InCl$_{4.8}$F$_{1.2}$ DHSE is understood by Nudged Elastic Band (NEB) calculations. Compared with Li$_3$InCl$_6$, F$^-$ in Li$_3$InCl$_{4.8}$F$_{1.2}$ has shorter and stronger bonds with lithium, and induces local distortion in the local Li coordination environment (Figure 1e). As a result, the changes in Li site energy with different Cl$^-$/F$^-$ coordination increases the barriers for Li-ion migration (Figure 1f). Reduced ionic conductivity of the F-introduced electrolyte is also observed in the reported F-doped sulfide SEs.[17] However, it is noted that the ionic conductivity of the Li$_3$InCl$_{4.8}$F$_{1.2}$ DHSE is significantly higher than that of all other reported fluoride-based SEs.[6b] The electronic
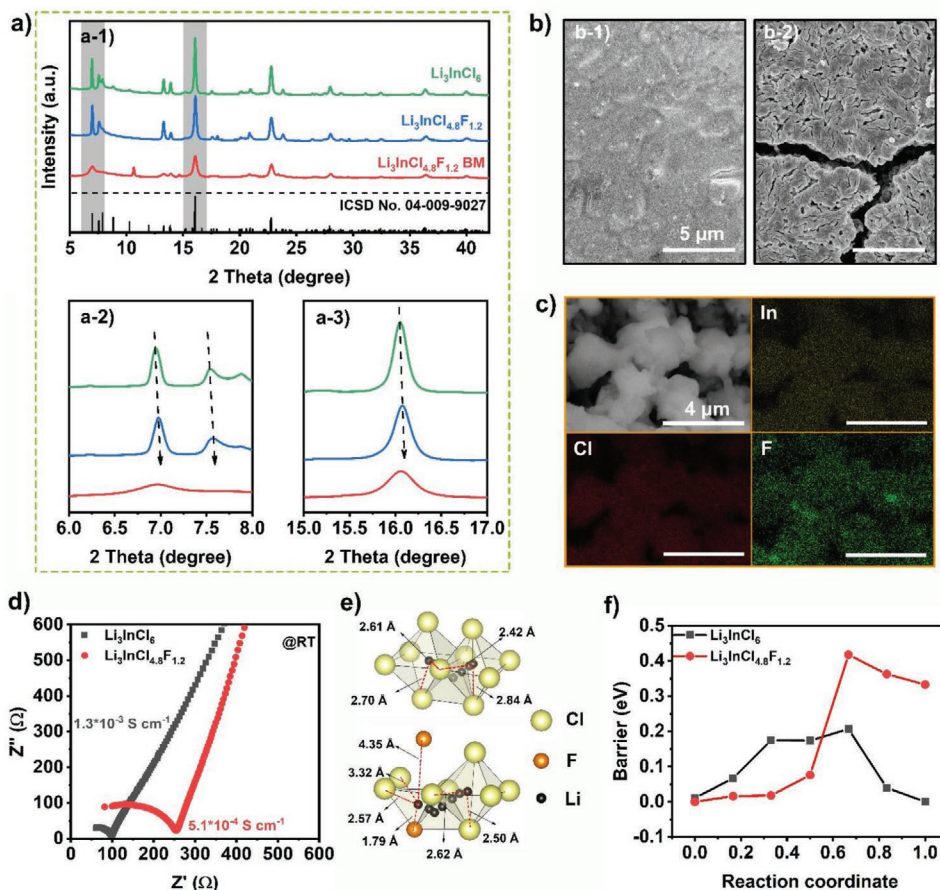
**ADVANCED
SCIENCE NEWS**
www.advancedsciencenews.com

**ADVANCED
ENERGY
MATERIALS**
www.advenergymat.de

Figure 1. a-1) SXRD ($\lambda = 0.729293$Å) patterns of the prepared $Li_3InCl_{4.8}F_{1.2}$ BM, $Li_3InCl_{4.8}F_{1.2}$, and Li_3InCl_6 powders and their corresponding magnified regions (a-2) 6° to 8° and a-3) 15° to 17°). b) SEM images of pelletized b-1) $Li_3InCl_{4.8}F_{1.2}$ DHSE and b-2) Li_3InCl_6 SE, scale bar: 5 μm. c) EDS elemental mapping of In, Cl, and F in the powder $Li_3InCl_{4.8}F_{1.2}$ sample, scale bar: 4 μm. d) Nyquist plots of Li_3InCl_6 and $Li_3InCl_{4.8}F_{1.2}$ SEs at room temperature (RT). e) The Li-ion migration pathways in the anion sublattice of Li_3InCl_6 (upper) and $Li_3InCl_{4.8}F_{1.2}$ (lower) structure, and f) corresponding energy profiles of Li-ion migration.

conductivity of the $Li_3InCl_{4.8}F_{1.2}$ was measured by a direct current (DC) polarization measurement (Figure S4, Supporting Information), which is 1.02×10^{-9} S cm^{-1}. Combining the advantages of chloride and fluoride SEs, it is anticipated that the $Li_3InCl_{4.8}F_{1.2}$ DHSE can serve as an essential component in cathode composite, which can not only provide enough Li-ion flux for essential electrochemical reactions, but also increase the practical anodic stability with the assistant of fluorinating components at the interface.

To understand the structure of $Li_3InCl_{4.8}F_{1.2}$ DHSE, Rietveld refinement was conducted using the SXRD pattern in Figure S5, Supporting Information, and the corresponding crystal structure is shown in **Figure 2**a. A distorted rock-salt structure belonging to the monoclinic group (C2/m) is observed. Anions (Cl$^-$ and F$^-$) are packed layer-by-layer to form edge-sharing octahedrons, where cation/vacancy fills each octahedral hole that is coordinated to six packing anion atoms. There are two symmetrically distinct Cl sites in $Li_3InCl_{4.8}F_{1.2}$, Cl3 (4i), and Cl6 (8j), and F is found to selectively occupy 16.2% of the Cl6 site. The detailed crystallographic data and atom occupation results are displayed in Tables S1 and S2, Supporting Information, respectively.

Due to the participation of F and its small radius, the unit cell parameters of $Li_3InCl_{4.8}F_{1.2}$ (a = 6.42009 Å, b = 11.07660 Å, c = 6.37873 Å) reduce and the corresponding cell volume shrinks to 427.32 Å^3. The doping of F was also confirmed by F K-edge XAS. The spectrum arises from the photo-excited transitions of F 1s→2p,[18] reflecting the local structure and bonding environment of F with the neighboring atoms. The corresponding changes can be determined by the shift of edge jump or the position of the first resonance (known as the whiteline[19]). As shown in Figure 2b, multiple scattering features of F K-edge XAS of $Li_3InCl_{4.8}F_{1.2}$ resemble those for LiF, indicating F in the DHSE exists in a similar octahedral environment to that of LiF.[20] However, compared to the spectra of LiF in the zoom-in figure, the whiteline of $Li_3InCl_{4.8}F_{1.2}$ shifts slightly to low energy (≈0.4 eV) due to F bonding contribution with indium, which can be further confirmed by their derivative absorption spectrum in Figure S6, Supporting Information. Therefore, co-existence of Li-F and In-F bonding is verified in the structure of $Li_3InCl_{4.8}F_{1.2}$. In addition, the structural stability of $Li_3InCl_{4.8}F_{1.2}$ was identified via first-principles calculations (see Tables S3 and S4, Supporting Information). Based on the XRD refinement results of
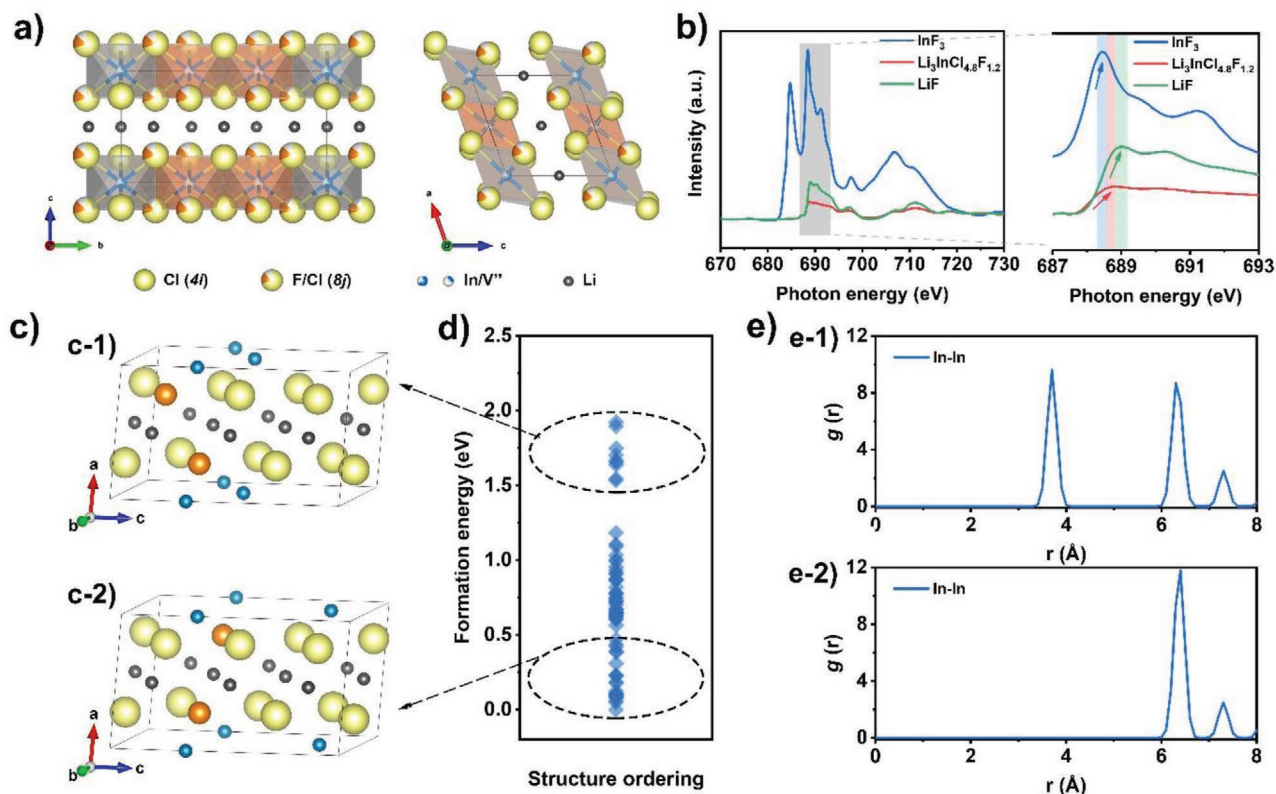
Figure 2. a) Crystal structure of $Li_3InCl_{4.8}F_{1.2}$ from the view that is parallel to a-axis and b-axis, respectively. b) F K-edge XAS spectra at $Li_3InCl_{4.8}F_{1.2}$ and standard samples (LiF and InF_3). First-principles calculations results: c) $Li_3InCl_{4.8}F_{1.2}$ unit cells with c-1) high-energy and c-2) low-energy In-F sublattice. d) Calculated formation energy of two In-F disordering in $Li_3InCl_{4.8}F_{1.2}$ versus the structure ordering which is referenced to the lowest-energy structure unit cell. e) In-In pair correlation function $g(r)$ for e-1) high-energy and e-2) low-energy structures.

$Li_3InCl_{4.8}F_{1.2}$, all the possible structures and site occupations in a primitive cell were enumerated and evaluated using DFT calculations. Uniform and sparse In^{3+} distribution to reduce Coulombic repulsion is observed in low-energy structures as shown in Figure 2c–e, which would benefit lithium diffusion by minimizing the effect of cation repulsion and blocking.[5c,21] The low-energy structures also have F ions occupy the diagonal 8j sites of In-centered octahedron, which agrees with the structures determined by the experiments in $Li_3InCl_{4.8}F_{1.2}$. These results provide systematical information that F successfully substitutes partly of Cl to form $Li_3InCl_{4.8}F_{1.2}$ DHSE.

2.2. Electrochemical Stability

The electrochemical stability of SEs is evaluated by the linear sweep voltammetry (LSV) with an asymmetric cell using carbon black (CB)/SE composites as the working electrode and lithium metal as the counter/reference electrode. The introduced CB in the working electrode can provide sufficient electron transport, thus precisely monitoring the reaction potentials.[22] **Figure 3**a shows the anodic (positive) scan curve (scan rate: 0.1 mV s^{-1}) of the cells with CB/$Li_3InCl_{4.8}F_{1.2}$ and CB/Li_3InCl_6 working electrodes. For the $Li_3InCl_{4.8}F_{1.2}$ cell,
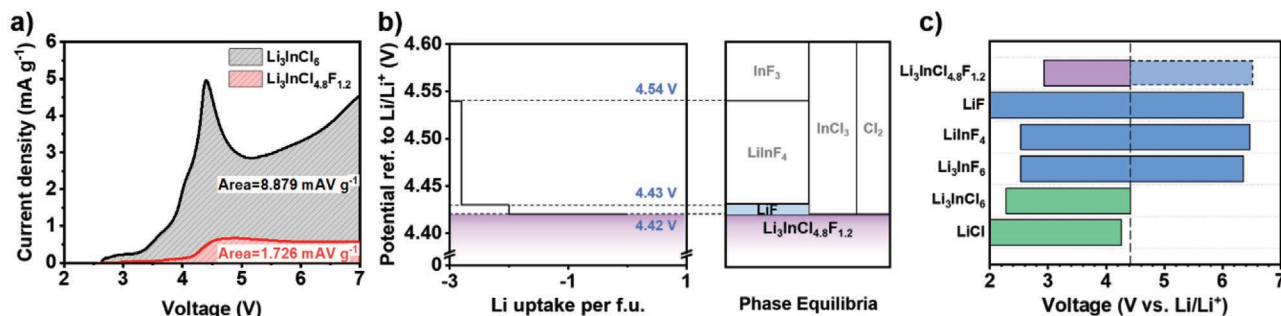

Figure 3. a) LSV analysis of the Li_3InCl_6 SE and $Li_3InCl_{4.8}F_{1.2}$ DHSE from the open-circuit voltage (OCV) to 7 V. The dashed area represents the integral spectrum intensity of each material. b) Phase equilibria of $Li_3InCl_{4.8}F_{1.2}$ DHSE at different Li/Li^+ potentials based on the first principles computation. c) The calculated thermodynamics electrochemical stability windows of $Li_3InCl_{4.8}F_{1.2}$, LiF, $LiInF_4$, In_3InF_6, Li_3InCl_6, and LiCl.

**ADVANCED
SCIENCE NEWS**
www.advancedsciencenews.com

**ADVANCED
ENERGY
MATERIALS**
www.advenergymat.de

the anodic potential is defined[23] to be ≈4.3 V, from which a negligible Faradaic current appears due to the oxidation reaction at the electrode. Notably, the LSV curve exhibits a plateau with the anodic current as small as 0.6 mA g^{-1} in the following potential range (≈4.3–7 V). This constant small current is probably due to the Nonfaradaic current which is caused by the passivating interface established at the electrode.[24] In the subsequent second anodic scan, the I-V curve is linear and no oxidation peaks are found (Figure S7, Supporting Information), further verifying that the in situ generation of a passivating interface during the first LSV process is stable and can prevent further interfacial reactions between the $Li_3InCl_{4.8}F_{1.2}$ DHSE and CB. In sharp contrast, the onset potential of the Li_3InCl_6 cell occurs prior to that of the $Li_3InCl_{4.8}F_{1.2}$ cell and the oxidation of Li_3InCl_6 becomes increasingly serious from ≈4.3 to 7 V, suggesting continuous and severe degradation of the Li_3InCl_6 SE. Moreover, the anodic stability difference is quantified by integrating the current density from 2.6–7 V. The integrated current of $Li_3InCl_{4.8}F_{1.2}$ is 1.726 mAV g^{-1}, which is one-fifth smaller than that of Li_3InCl_6, indicating significantly improved anodic stability of the $Li_3InCl_{4.8}F_{1.2}$ DHSE.

First-principles computation was employed to understand the enhanced electrochemical stability of $Li_3InCl_{4.8}F_{1.2}$ DHSE again CB at varying applied voltages. Based on the thermodynamic equilibrium voltage profile (Figure S8, Supporting Information), the calculated anodic potential of $Li_3InCl_{4.8}F_{1.2}$ DHSE is 4.42 V, which is close to the experimental value where oxidation begins to happen in Figure 3a. Despite the oxidation potential of the $Li_3InCl_{4.8}F_{1.2}$, DHSE itself depends on the redox of Cl (-1)/Cl (0) at 4.42 V, its practical anodic limit, and the practical electrochemical window are dominated by the in situ derived passivating interface. Figure 3b depicts the calculated phase equilibrium of $Li_3InCl_{4.8}F_{1.2}$ DHSE at different Li/Li$^+$ potentials. The pre-stored F in $Li_3InCl_{4.8}F_{1.2}$ DHSE near the interface contributes to the formation of fluorinating interphase.[25] Specifically, LiF is expected to first generate once the oxidation of DHSE occurs, followed by $LiInF_4$ and InF_3 at around 4.43 and 4.54 V, respectively. The thermodynamic electrochemical stability window and anodic limit of F-containing compounds (such as LiF, $LiInF_4$, and $LiInF_6$) are calculated in Figure 3c. All of them feature a wide electrochemical stability window with ultrahigh anodic limits > 6 V, thus these F-containing compounds are key components for passivating interphase layers. Together, these reaction products enable an extended electrochemical stability window to compensate for the thermodynamic intrinsic anodic limit of $Li_3InCl_{4.8}F_{1.2}$ DHSE to achieve an ultrahigh anodic limit over 6 V. In consistency with the LSV observations, the formation of F-containing passivating interphases protect $Li_3InCl_{4.8}F_{1.2}$ DHSE from further decomposition and strengthen its oxidation stability.

2.3. Full Battery Performance

To demonstrate the applicability of the $Li_3InCl_{4.8}F_{1.2}$ DHSE in high-voltage ASSLIBs, we utilized $Li_3InCl_{4.8}F_{1.2}$ as cathode electrolyte, matching a commercialized high-voltage LCO (designed cut-off voltage: 4.47 V) to fabricate bulk-type

halide-based ASSLIBs. It is noted that the liquid-electrolyte half-cell using the high-voltage LCO as the cathode material was first assembled, and the cycling stability was evaluated as shown in Figure S9, Supporting Information. The negligible capacity decay during 100 cycles indicates the good structural stability of the high-voltage LCO cathode material. Room-temperature galvanostatic measurements were conducted on the In//Li$_6$PS$_5$Cl//Li$_3$InCl$_6$/Li$_3$InCl$_{4.8}$F$_{1.2}$/LCO all-solid-state full cells in the voltage range of 2.6–4.47 V (vs Li/Li$^+$). **Figure 4**a depicts the charge and discharge profiles of the full cell in the first three cycles at a low current density of 0.063 mA cm^{-2}. An initial reversible specific capacity of 160.6 mAh g^{-1} is achieved with a high Coulombic efficiency of 92%. The cyclic voltammetry (CV) test for the ASSLIB was conducted to exhibit the highly reversible lithiation and de-lithiation process (Figure S10, Supporting Information). Additionally, the cycling performance of ASSLIBs with different cathode electrolytes is depicted in Figure 4b. It is obvious to find that the cycling stability of the cell with $Li_3InCl_{4.8}F_{1.2}$ is remarkably improved in comparison with the full cell using Li_3InCl_6 as the electrolyte in the cathode composite. The reversible specific capacity slightly drops to 140.0 mAh g^{-1} after the initial five cycles and a value of 102 mAh g^{-1} can be retained after 70 cycles. Notably, the average Coulombic efficiency reaches 99.5% during this long cycling process, confirming highly reversible Li-ion intercalation/de-intercalation behavior once the stabilized and Li-ion conductive passivation layer forms. Furthermore, Galvanostatic intermittent titration technique (GITT) was employed to verify the low polarization of Li-ion (de)intercalation toward the LCO cathode materials in the presence of $Li_3InCl_{4.8}F_{1.2}$ DHSE (Figure S11a, Supporting Information). The Columbic efficiency of the GITT charge-discharge process reaches as high as 89%, suggesting a good charge/discharge reversibility of the full cells.[26] The cathode composite with $Li_3InCl_{4.8}F_{1.2}$ shows lower polarization than that with Li_3InCl_6 during the discharging process, which indicates the interfacial stability between $Li_3InCl_{4.8}F_{1.2}$ and LCO. (Figure S11b, Supporting Information). To fully utilize the high practical anodic stability of $Li_3InCl_{4.8}F_{1.2}$ DHSE, a rigorous charging protocol with a cut-off voltage of 4.8 V (vs Li/Li$^+$) was applied to the $Li_3InCl_{4.8}F_{1.2}$ cell. The comparison of charge-discharge behaviors between $Li_3InCl_{4.8}F_{1.2}$ and Li_3InCl_6 cells is exhibited in Figure 4c. $Li_3InCl_{4.8}F_{1.2}$ cell delivers a reversible capacity of 203.7 mAh g^{-1} with the initial Columbic efficiency of 89.2%, higher than that of the Li_3InCl_6 cell. After a low-rate activation process, the capacity of Li_3InCl_6 cell drops, and the polarization dramatically increases at 10th and 20th cycles, while the $Li_3InCl_{4.8}F_{1.2}$ cell maintains a decent cycling performance over 70 cycles (Figure 4d) despite the capacity decay possibly caused by the structural instability of LCO materials over 4.47 V. These results further prove the excellent interfacial stability between LCO and $Li_3InCl_{4.8}F_{1.2}$, which evokes the high capacity of LCO cathode materials at high voltages. To the best of our knowledge, the aforementioned high cut-off voltage is higher than any reported charging protocols previously reported with LCO-based cathode materials, and the delivered capacity, as well as the durability, both are among the best-reported performances in the high-voltage ASSLBs field (Table S5, Supporting Information).
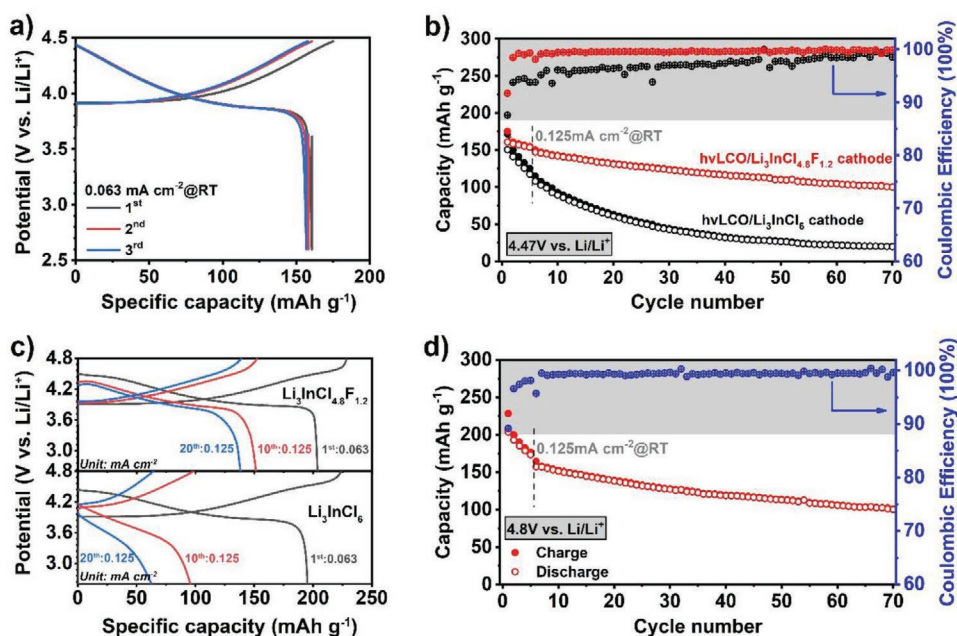
ADVANCED
SCIENCE NEWS
www.advancedsciencenews.com

ADVANCED
ENERGY
MATERIALS
www.advenergymat.de

Figure 4. Electrochemical performance of the full cells using $Li_3InCl_{4.8}F_{1.2}$ and Li_3InCl_6 cathode SE. a) the first three discharge/charge curves of $Li_3InCl_{4.8}F_{1.2}$ cathode SE cell. b) Cycling performance of $Li_3InCl_{4.8}F_{1.2}$ and Li_3InCl_6 cathode SE cells in the voltage range of 2.6–4.47 V (vs Li/Li+) (first 5 cycles at 0.063 mA cm^{-2}). c) Charge-discharge profiles of $Li_3InCl_{4.8}F_{1.2}$ (upper) and Li_3InCl_6 (lower) cathode SE cells at 1st, 10th, and 20th cycles in the voltage range of 2.6–4.8 V (vs Li/Li+). d) Cycling performance of $Li_3InCl_{4.8}F_{1.2}$ cathode SE cell charged at 4.8 V (vs Li/Li+) (first 5 cycles at 0.063 mA cm^{-2}).

2.4. Mechanism Behind High-Voltage Stability

A fundamental understanding behind the nature of the high-voltage-stable passivation layer was achieved via various spectroscopic, thermodynamic, and electrochemical characterizations. **Figure 5**a depicts the F K-edge XAS of the cycled

LCO/$Li_3InCl_{4.8}F_{1.2}$ cathode composites (after 1 cycle and 10 cycles) in fluorescence yield (FLY) mode. They show similar six-coordinating features in the extended spectral region compared with the pristine $Li_3InCl_{4.8}F_{1.2}$ DHSE. Precise identification is shown in a magnified plot in Figure S12, Supporting Information. The 1-cycle and 10-cycle LCO/$Li_3InCl_{4.8}F_{1.2}$ samples have

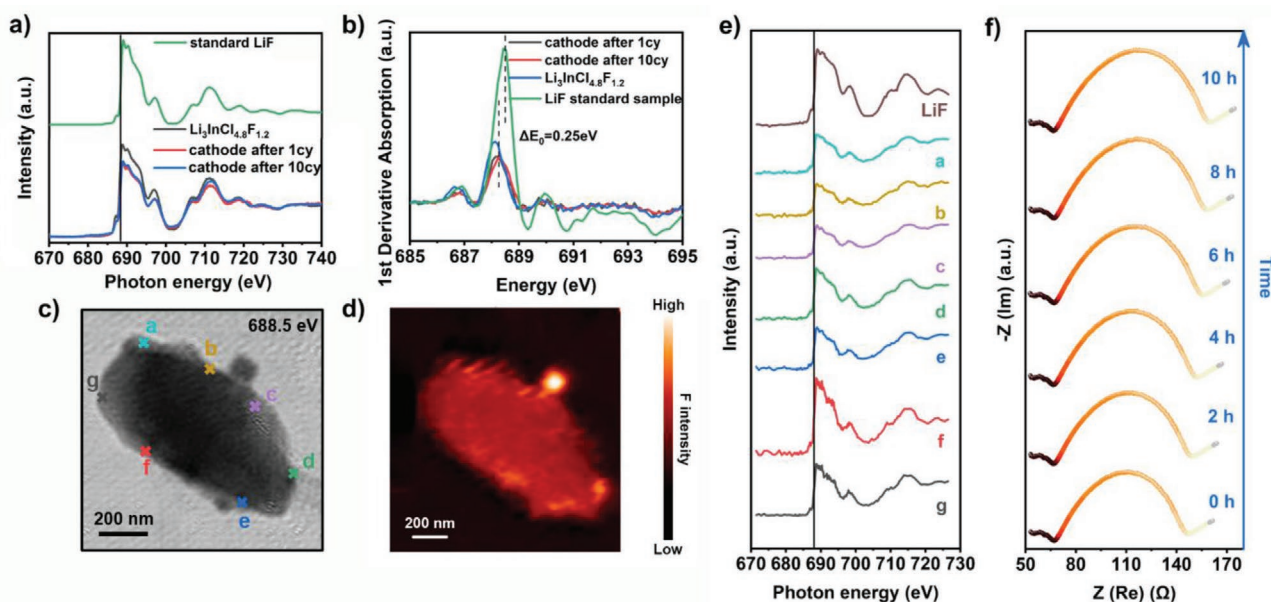**Figure 5.** Synchrotron spectroscopic analyses for standard LiF, $Li_3InCl_{4.8}F_{1.2}$, and LCO/$Li_3InCl_{4.8}F_{1.2}$ cathode composites after 1st, 10th, and 50th cycling processes: a) F K-edge XAS (the E_0 of standard LiF is marked by the black vertical line) and b) first derivative absorption spectra. c) X-ray ptychography and d) STXM mapping images of a single 50-cycle LCO particle at 688.5 eV, pixel size: 5.7 nm. e) F K-edge XAS at 7 marked positions (a–g) in (c) compared with that of the standard LiF. f) The periodic EIS results during a CVC test process at 4.47 V, time scale indicates the time of CVC processes.

**ADVANCED
SCIENCE NEWS**
www.advancedsciencenews.com

**ADVANCED
ENERGY
MATERIALS**
www.advenergymat.de

the same absorption threshold (E_0) and whiteline position, but blue-shift compared with the F K-edge spectrum of the pristine $Li_3InCl_{4.8}F_{1.2}$ DHSE. This suggests that a passivating CEI is electrochemically generated after the first cycle and maintains stability in the subsequent cycles. In comparison with the standard LiF (E_0 is marked by black vertical line),[27] both two cycled samples (1-cycle and 10-cycle) show a low-energy-shift (redshift) absorption edge, which can be tracked in the first derivative XAS plot (Figure 5b) and quantified as 0.25 eV, providing further evidence that a considerable amount of LiF is probably generated as the component of the CEI layer. The flat F K-pre-edge feature also suggests the existence of rather weak metal-ligand bonds, excluding the generation of $LiInF_4$ and InF_3.[28] In order to further identify the distribution and composition of the CEI, synchrotron-based STXM was utilized to measure the transmitted intensity at 50-cycle LCO particles.[29] As shown in Figure S13, Supporting Information, A single LCO particle (dark area) was first screened in conventional STXM at the photon energy of 780 eV (the energy of Co L-edge). Then, STXM-ptychography technique[30] is adopted, which demonstrates high-resolution transmission images of the single LCO particle in the photon energy between 681.5 and 691.5 eV (Figure S14, Supporting Information). A reconstructed image at the photon energy of 688.5 eV (close to the absorption energy of F K-edge) is picked and displayed in Figure 5c. STXM mapping of F shown in Figure 5d visualizes the CEI layer in situ formed on one single LCO particle, which displays a relatively homogenous distribution of F on the cathode surface. Such distributions proceed from F K-edge absorption spectra via conventional STXM mode, which provides detailed information for the CEI composition. Various positions (marked from a to g in Figure 5c) were selected around the LCO particle and the corresponding spectra of F K-edge are plotted in Figure 5e. It is found that the seven spectra have same E_0 as that of the standard LiF, revealing that LiF is the major compound of the in situ generated CEI layer. In addition, thermodynamic analyses based on first principles computation[12,14b] were applied to study the LCO/$Li_3InCl_{4.8}F_{1.2}$ interface at charged and discharged states. As shown in **Table 1**, the minimum mutual reaction energies ($\Delta E_{D, min, mutual}$) of $Li_3InCl_{4.8}F_{1.2}$ against LCO are as small as −15 meV at discharged (lithiation) state and −7 meV at charged (delithiation) state, respectively. The calculated

phase equilibria components of LCO/$Li_3InCl_{4.8}F_{1.2}$ are largely similar to those of the LCO/Li_3InCl_6 interface; however, the major difference is that the side-reaction products of LCO/$Li_3InCl_{4.8}F_{1.2}$ contain LiF. The excellent stability of LiF against LCO can be quantified as 0 meV decomposition energy both in charged and discharged states, thus leading to the enhanced interfacial stability of LCO/$Li_3InCl_{4.8}F_{1.2}$, especially under ultra-high-voltage status.

To further demonstrate the high-voltage stability of $Li_3InCl_{4.8}F_{1.2}$ DHSE in ASSLIBs, we designed a constant-voltage protocol to monitor the impedance change of a full cell during an aging process at high-voltage status. Once the full cell was charged to 4.47 V (vs Li/Li$^+$), a periodic 2-h constant-voltage charging (CVC) and 2-h rest (to equilibrium state) were applied then followed by EIS measurements. The according EIS plots after the periodic rests are displayed in Figure 5f. The total impedance in each period shows negligible changes and almost keeps the same value of ≈150 Ω, indicating the F-rich CEI layer formed in the initial charging process effectively prevents further interfacial reactions between the $Li_3InCl_{4.8}F_{1.2}$ DHSE and fully charged LCO cathode. Combining the findings from the abovementioned discussions, $Li_3InCl_{4.8}F_{1.2}$ DHSE is demonstrated to show great potential in ultrahigh-voltage ASSLIBs, which can be achieved by transforming the contact surface of $Li_3InCl_{4.8}F_{1.2}$ DHSE into an F-rich CEI layer to stabilize the cathode material/DHSE interface at high operating voltages.[31]

3. Conclusion

In summary, we developed a DHSE that can enable ultrahigh-voltage ASSLIBs. F is introduced in a halide SE and selectively occupies part of the Cl sites to form a morphologically dense $Li_3InCl_{4.8}F_{1.2}$ DHSE, which shows a good ionic conductivity of 5.1×10^{-4} S cm^{-1} at RT and high practical anodic stability over 6 V. Both experimental and computational results identify that F-containing passivating components are generated from $Li_3InCl_{4.8}F_{1.2}$ DHSE at an applied potential, protecting the $Li_3InCl_{4.8}F_{1.2}$ from further decomposition and extending its anodic stability window. As a proof of concept, this $Li_3InCl_{4.8}F_{1.2}$ DHSE is demonstrated in high-voltage ASSLIBs, performing good cycling stability at RT. Spectroscopic, computational, and

Table 1. Phase equilibria and minimum decomposition energies of the $Li_3InCl_{4.8}F_{1.2}$, Li_3InCl_6, LiF, $LiInF_4$, and Li_3InF_6 materials at the interface with $LiCoO_2$ cathode materials under charged and discharged status.

C_{SE}	LCO cathode status	x_m	Phase equilibria at x_m	$\Delta E_{D,min,mutual}$ [meV atom^{-1}]
$Li_3InCl_{4.8}F_{1.2}$	discharged	0.83	$Li(CoO_2)_2$, InClO, Co_3O_4, Li_3InCl_6, LiF	−15
	charged	0.77	$LiClO_4$, InClO, Co_3O_4, Li_3InCl_6, LiF	−7
Li_3InCl_6	discharged	0.5	$Li(CoO_2)_2$, InClO, Co_3O_4, LiCl	−4
	charged	–	$Li(CoO_2)_2$, Li_3InCl_6 (stable)	0
LiF	discharged	–	$LiCoO_2$, LiF (stable)	0
	charged	–	$Li(CoO_2)_2$, LiF (stable)	0
$LiInF_4$	discharged	0.29	In_2O_3, Co_3O_4, $Li(CoO_2)_2$, LiF	−51
	charged	–	$Li(CoO_2)_2$, $LiInF_4$ (stable)	0
Li_3InF_6	discharged	0.40	In_2O_3, Co_3O_4, $Li(CoO_2)_2$, LiF	−43
	charged	–	$Li(CoO_2)_2$, Li_3InF_6 (stable)	0

**ADVANCED
SCIENCE NEWS**

www.advancedsciencenews.com

**ADVANCED
ENERGY
MATERIALS**

www.advenergymat.de

electrochemical characterizations are utilized to deeply understand the practical electrochemical stability of $Li_3InCl_{4.8}F_{1.2}$ and high-voltage stability of full cells. Rich F-containing passivating interphases are proved to generate in situ on the cathode interface and prevent further interfacial reactions at high-voltages, contributing to promising cycling stability in full cells. This work presents a new DHSE with outstanding practical anodic stability, paving the way for rapid development and wide application of all-solid-state batteries at ultrahigh operational voltages.

4. Experimental Section

Synthesis of Li_3InCl_6 and $Li_3InCl_{4.8}F_{1.2}$ Solid Electrolytes: All raw materials were purchased and used directly as received. LiCl (Sigma-Aldrich, ≥99.98% trace metals basis), $InCl_3$ (Sigma-Aldrich, 98%), and InF_3 (Alfa Aesar anhydrous, 99.95% (metals basis)) were used as precursors and they were mixed with a stoichiometric amount in an argon-filled glovebox. The resulting mixture (≈1 g) was then placed in a zirconia ball milling pot along with 40 g zirconia balls. Low-speed ball milling (150 rpm for 2 h) was first run to ensure all the precursors mixed well, followed by a high-speed ball milling process of 500 rpm for 20 h. Next, the ball-milled product was pelletized and sealed in quartz tubes for annealing under 260 °C for 5 hrs. After naturally cooling down to RT, the SE pellets were transferred into the glovebox and manually ground into powders for further use.

Ionic Conductivity and Porosity Measurements: The porosity measurement as a function of applied pressure was similar to previous reports.[11,32] Ionic conductivity of as-prepared SEs was evaluated by using electrochemical impedance spectroscopy (EIS) with two stainless steel rods as blocking electrodes. The SE powders were cold-pressed into pellets under ≈400 Mpa. EIS measurements were performed using a multichannel potentiostation 3/Z (German VMP3). The applied frequency range was ≈1 Hz–7 MHz and the amplitude was 20 mV. DC polarization measurements were conducted on a pellet with applied voltages of 0.1, 0.2, 0.3, 0.4, and 0.5 V for 60 min each to determine the electronic conductivity of $Li_3InCl_{4.8}F_{1.2}$ DHSE.

LSV Testing Cells: Two kinds of SE powders (Li_3InCl_6 and $Li_3InCl_{4.8}F_{1.2}$) were first manually mixed well with carbon black (CB) at a ratio of 8:2, respectively. Then, 80 mg of Li_3InCl_6 powder was cold-pressed into a pellet under a pressure of 300 MPa. 10 mg of SE/CB mixture was uniformly placed on one side of the Li_3InCl_6 pellet as working electrode and compressed again under the same pressure. After that, Li foil (China Energy Lithium Co. LTD) was attached on the other side of the pellet as both counter and reference electrode. In order to avoid the incompatibility between Li_3InCl_6 and metallic Li, a thinner layer of sulfide SE (Li_6PS_5Cl: ≈40 mg)[33] was inserted between the Li_3InCl_6 pellet and Li before Li foil was added. To ensure an intimate contact between layer by layer, the cell was pressed under a pressure of ≈120 MPa before taking out of the glovebox. The LSV electrochemical stability window tests were conducted using versatile multichannel potentiostat 3/Z (VMP3) with a scan range from open-circuit voltage (OCV) to 7 V (vs Li/Li+). The scan rate was 0.1 mV s⁻¹.

ASSLIBs: For the cathode composite, two kinds of SE powders (Li_3InCl_6 and $Li_3InCl_{4.8}F_{1.2}$) were manually mixed for over 15 min with high-voltage lithium cobalt oxide (LCO) at a ratio of 3:7, respectively. The high-voltage LCO was supplied from China Automotive Battery Research Institute. The powder has a PSD-D50 of ≈16 μm and a BET-specific surface area of 0.190 m² g⁻¹. The particles were neither agglomerated nor coagulated. The total procedure was similar to above for LSV testing but Li foil was changed to In foil (99.99%, Φ 10 mm, thickness 0.1 mm). Typically, 80 mg of Li_3InCl_6 powder was cold-pressed into a pellet under a pressure of 300 MPa. 10 mg of the cathode composite was uniformly placed on one side of the Li_3InCl_6 pellet and compressed again under the same pressure. After that, In foil was attached on the other side before adding a thinner layer of sulfide SE (Li_6PS_5Cl: ≈40 mg) between Li_3InCl_6 pellet and In to avoid the possible influence of redox conversion between In^{3+} and In foil. The cell was pressed under a pressure of ≈120 MPa

before taking out of the glovebox. Galvanostatic charge-discharge was conducted on a LAND battery test system. The voltage window was set as 2.6–4.47 and 4.8 V (vs Li/Li+) to evaluate the cycling stability and the rate performance. Cyclic voltammetry (CV) measurements were conducted using versatile multichannel potentiostat 3/Z (VMP3) under a voltage profile of 2.6–4.47 V (vs Li/Li+) at a scan rate of 0.1 mV s⁻¹. The GITT was employed to analyze the apparent chemical reactions between electrolyte and electrode. The batteries were charged/discharged 1 cycle at a current of 0.05 C for 30 min and followed by 4 h relaxation until the voltage reached upper or lower limits.

Characterization Methods: SXRD measurements were performed at beamline 33-BM-C at the Advanced Photon Source (APS) of Argonne National Laboratory using a constant wavelength of 0.729293 Å. The use of high-energy X-rays (E = 21 keV) minimizes absorption effects. The Rietveld refinements were performed using the TOPAS 5.0 software package (Bruker). The powder samples were packed and sealed into Kapton tape to avoid air exposure. SEM images and element mapping were obtained by using a Hitachi S-4800 field-emission scanning electron microscope (FE-SEM, acceleration voltage 5 kV) equipped with energy dispersive spectroscopy (EDS). X-ray absorption spectroscopy (XAS) measurements were conducted at the SGM beamline (11ID-1, 250–2000 eV) of Canadian Light Source (CLS). For LiF and InF_3 standard samples, absorption was measured using drain current in total electron yield (TEY) mode. The absorption of all the experimental samples was collected in FLY mode. STXM was carried out on the soft X-ray spectromicroscopy (SM, ≈130–2700 eV) beamline at CLS. The LCO/$Li_3InCl_{4.8}F_{1.2}$ cathode composite powder (after 50 cycles) was ultrasonically dispersed in heptane for over one hour. SGM and STXM data were processed with Athena and aXis2000 softwares.

Sites Occupancy Ordering: The $Li_3InCl_{4.8}F_{1.2}$ sample can be indexed well with a distorted monoclinic rock-salt structure with the C2/m space group as Li_3InCl_6 (ICSD No. 89 617), which has the partial occupancy of In at 4g/2a sites and F at 8j sites. To determine the site's occupancy, the same ordering procedure was employed as in previous studies.[12,34] Based on the structure and site occupancies from XRD refinement results, all the possible structures were enumerated in a primitive cell at the composition of Li_3InCl_5F using the pymatgen package.[35] And then all the 69 symmetry-independent structures were statically relaxed in the DFT calculations. The lowest energy structure was identified as the ground state for other further calculations. The In ions tend to have a uniform distribution to have further distances to reduce Coulomb repulsion as the In-In pair correlation function for several low-energy structures in Figure 2c.

Electrochemical Stability: The phase diagram was constructed to evaluate the stability of a material in equilibrium against external environment.[36] To study the electrochemical stability, the grand phase equilibria of solid electrolyte was identified in equilibrium with Li reservoir at chemical potential μ_{Li} referenced to Li metal. As in previous studies,[37] the decomposition reaction energy at a given chemical potential μ_{Li} of element Li was calculated as:

$$\Delta E_D^{open}(phase, \mu_{Li}) = E_{eq}\left(C_{eq}(C, \mu_{Li})\right) - E(phase) - \Delta n_{Li} \cdot \mu_{Li} \tag{1}$$

Where $C_{eq}(C, \mu_{Li})$ is the phase equilibria of a given phase composition C at the given chemical potential of μ_{Li}. The electrochemical window of the phase was estimated as the range of μ_{Li}, where the phase was neither oxidized nor reduced.

Interface Stability: The interface was considered as a pseudo-binary of the solid electrolyte and the electrode as in previous study.[14b,37] The interface phase equilibria were evaluated along the energy minimum using the decomposition energy ΔE_D in the previous studies:

$$\Delta E_D(SSE, electrode, x) = E_{eq}\left(C_{interface}(C_{SE}, C_{electrode}, x)\right) - E_{interface}(SE, electrode, x) \tag{2}$$

where C_{SE} and $C_{electrode}$ are the compositions of SSE and electrode materials at the interface, normalized to one atom per formula. The

x is the molar fraction of the SSE, since the phase equilibria and the reaction energies vary with the pseudo-binary composition, the minimum of the reaction energy ($\Delta E_{D,min}$) at molar fraction of x_m was identified in the study. The $\Delta E_{D,min,mutual}$ and $\Delta E_{D,min,toal}$ represent minimum interface decomposition energy excluding and including the decomposition energy of the SE and electrode, respectively. The energies of decomposed materials were obtained from MP database, and more details can be found in previous studies.[14b,37] $LiCoO_2$ and $Li_{0.5}CoO_2$ were considered as the discharged and charged states of the cathode material, respectively.[14b]

Ab Initio Molecular Dynamics Simulation (AIMD): AIMD simulation was performed as the previous scheme.[36b] The supercells with lattice parameters larger than 10 Å in each direction, non-spin mode, and Γ-centered $1 \times 1 \times 1$ k-point grid were used. The initial temperature of simulations was set to 100 K and then the structures were heated to the target temperatures at a constant rate by velocity scaling during a period of 2 ps. All simulations adopted the NVT ensemble with Nosé–Hoover thermostat.[38] The lithium ionic conductivity was calculated following the Nernst–Einstein relation as:

$$\sigma = \frac{N}{V}\frac{q^2}{k_B T}D = \frac{q^2}{V k_B T}\frac{TMSD(\Delta t)}{2d\Delta t} \tag{3}$$

where N is the number of the mobile carriers and d is the diffusion dimensionality which is 3 in the simulation, V is the volume of the model, q is the charge of the carrier, k_B is the Boltzmann constant, and T is the temperature, total mean square displacement (TMSD) represents the total diffusion of all lithium ions in the material. Arrhenius relation was used to get diffusion barrier and to evaluate the ionic conductivity at desired temperature

$$\sigma T = \sigma_0 \exp\left(\frac{-E_a}{k_B T}\right) \tag{4}$$

where E_a is the activation energy, σ_0 is the pre-exponential factor. Given that ion hopping is a stochastic process, the statistical deviations of the diffusivities were evaluated according to the values of TMSD in the previous report.[39] The total time duration of AIMD simulations was within the range of 100 to 300 ps until the ionic diffusivity converged with a relative standard deviation is from 20 to 30%.

Nudged Elastic Band Calculations (NEB): NEB[40] calculation was performed for Li hopping between two adjacent octahedral sites through the intermediate tetrahedral sites, the only diffusion pathway observed in the AIMD. A Li-ion was removed from the original structure to create a vacancy for Li-ion hopping with a background electron for charge compensation. Static relaxation was done for initial and final structures with the same supercell, the energy convergence criterion was set to 10^{-7} eV and a force convergence criterion was set to 0.01 eV Å^{-1}. And then five images were linearly interpolated between the initial and final structure for NEB calculation. The energy convergence criterion in NEB calculation was adjusted to 10^{-5} eV and the force convergence criterion was set to 0.05 eV Å^{-1}. The energy barrier ΔE_b was calculated by the difference between the maximum and minimum energies along the entire oct-tet-oct migration pathway.

Supporting Information

Supporting Information is available from the Wiley Online Library or from the author.

Acknowledgements

Conflict of Interest

The authors declare no conflict of interest.

Data Availability Statement

Research data are not shared.

Keywords

[1] a) Q. Zhao, S. Stalin, C. Z. Zhao, L. A. Archer, *Nat. Rev. Mater.* **2020**, *5*, 229; b) R. S. Chen, Q. H. Li, X. Q. Yu, L. Q. Chen, H. Li, *Chem. Rev.* **2020**, *120*, 6820.

[2] a) M. Li, C. S. Wang, Z. W. Chen, K. Xu, J. Lu, *Chem. Rev.* **2020**, *120*, 6783; b) W. Zhao, J. Yi, P. He, H. Zhou, *Electrochem. Energy Rev.* **2019**, *2*, 574.

[3] a) Q. Zhang, D. X. Cao, Y. Ma, A. Natan, P. Aurora, H. L. Zhu, *Adv. Mater.* **2019**, *31*, 1901131; b) N. Kamaya, K. Homma, Y. Yamakawa, M. Hirayama, R. Kanno, M. Yonemura, T. Kamiyama, Y. Kato, S. Hama, K. Kawamoto, A. Mitsui, *Nat. Mater.* **2011**, *10*, 682; c) Y. Kato, S. Hori, T. Saito, K. Suzuki, M. Hirayama, A. Mitsui, M. Yonemura, H. Iba, R. Kanno, *Nat. Energy* **2016**, *1*, 16030.

[4] a) A. Manthiram, X. W. Yu, S. F. Wang, *Nat. Rev. Mater.* **2017**, *2*, 16103; b) Y. H. Xiao, Y. Wang, S. H. Bo, J. C. Kim, L. J. Miara, G. Ceder, *Nat. Rev. Mater.* **2020**, *5*, 105.

[5] a) T. Asano, A. Sakai, S. Ouchi, M. Sakaida, A. Miyazaki, S. Hasegawa, *Adv. Mater.* **2018**, *30*, 1803075; b) X. N. Li, J. W. Liang, J. Luo, M. N. Banis, C. H. Wang, W. H. Li, S. X. Deng, C. Yu, F. P. Zhao, Y. F. Hu, T. K. Sham, L. Zhang, S. Q. Zhao, S. G. Lu, H. Huang, R. Y. Li, K. R. Adair, X. L. Sun, *Energy Environ. Sci.* **2019**, *12*, 2665; c) J. Liang, X. Li, S. Wang, K. R. Adair, W. Li, Y. Zhao, C. Wang, Y. Hu, L. Zhang, S. Zhao, S. Lu, H. Huang, R. Li, Y. Mo, X. Sun, *J. Am. Chem. Soc.* **2020**, *142*, 7012; d) L. D. Zhou, C. Y. Kwok, A. Shyamsunder, Q. Zhang, X. H. Wu, L. F. Nazar, *Energy Environ. Sci.* **2020**, *13*, 2056.

**ADVANCED
SCIENCE NEWS**

www.advancedsciencenews.com

**ADVANCED
ENERGY
MATERIALS**

www.advenergymat.de

[6] a) X. N. Li, J. W. Liang, N. Chen, J. Luo, K. R. Adair, C. H. Wang, M. N. Banis, T. K. Sham, L. Zhang, S. Q. Zhao, S. G. Lu, H. Huang, R. Y. Li, X. L. Sun, *Angew. Chem., Int. Ed.* **2019**, *58*, 16427; b) J. L. Hu, Z. G. Yao, K. Y. Chen, C. L. Li, *Energy Storage Mater.* **2020**, *28*, 37.

[7] M. Feinauer, H. Euchner, M. Fichtner, M. A. Reddy, *ACS Appl. Energy Mater.* **2019**, *2*, 7196.

[8] R. Schlem, S. Muy, N. Prinz, A. Banik, Y. Shao-Horn, M. Zobel, W. G. Zeier, *Adv. Energy Mater.* **2020**, *10*, 1903719.

[9] X. N. Li, J. W. Liang, X. F. Yang, K. R. Adair, C. H. Wang, F. P. Zhao, X. L. Sun, *Energy Environ. Sci.* **2020**, *13*, 1429.

[10] K. H. Park, K. Kaup, A. Assoud, Q. Zhang, X. H. Wu, L. F. Nazar, *ACS Energy Lett.* **2020**, *5*, 533.

[11] H. Kwak, D. Han, J. Lyoo, J. Park, S. H. Jung, Y. Han, G. Kwon, H. Kim, S. T. Hong, K. W. Nam, Y. S. Jung, *Adv. Energy Mater.* **2021**, *11*, 2003190.

[12] S. Wang, Q. Bai, A. M. Nolan, Y. Liu, S. Gong, Q. Sun, Y. Mo, *Angew. Chem., Int. Ed.* **2019**, *58*, 8039.

[13] a) S. P. Culver, R. Koerver, W. G. Zeier, J. Janek, *Adv. Energy Mater.* **2019**, *9*, 1900626; b) Y. H. Xiao, L. J. Miara, Y. Wang, G. Ceder, *Joule* **2019**, *3*, 1252.

[14] a) Y. Zhao, K. Zheng, X. L. Sun, *Joule* **2018**, *2*, 2583; b) Y. Z. Zhu, X. F. He, Y. F. Mo, *J. Mater. Chem. A* **2016**, *4*, 3253.

[15] F. Mo, J. Ruan, S. Sun, Z. Lian, S. Yang, X. Yue, Y. Song, Y. N. Zhou, F. Fang, G. Sun, S. Peng, D. Sun, *Adv. Energy Mater.* **2019**, *9*, 1902123.

[16] a) J. Kang, B. Han, *J. Phys. Chem. Lett.* **2016**, *7*, 2671; b) K. Nam, H. Chun, J. Hwang, B. Han, *ACS Sustainable Chem. Eng.* **2020**, *8*, 3321.

[17] F. P. Zhao, Q. Sun, C. Yu, S. M. Zhang, K. Adair, S. Z. Wang, Y. L. Liu, Y. Zhao, J. W. Liang, C. H. Wang, X. N. Li, X. Li, W. Xia, R. Y. Li, H. Huang, L. Zhang, S. Q. Zhao, S. G. Lu, X. L. Sun, *ACS Energy Lett.* **2020**, *5*, 1035.

[18] Y. Gao, T. Tiedje, P. C. Wong, K. A. R. Mitchell, *Phys. Rev. B* **1993**, *48*, 15578.

[19] T. K. Sham, *Acc. Chem. Res.* **1986**, *19*, 99.

[20] B. Q. Wang, J. Liu, M. N. Banis, Q. Sun, Y. Zhao, R. Y. Li, T. K. Sham, X. L. Sun, *ACS Appl. Mater. Interfaces* **2017**, *9*, 31786.

[21] Y. S. Liu, S. Wang, A. M. Nolan, C. Ling, Y. F. Mo, *Adv. Energy Mater.* **2020**, *10*, 2002356.

[22] G. F. Dewald, S. Ohno, M. A. Kraft, R. Koerver, P. Till, N. M. Vargas-Barbosa, J. Janek, W. G. Zeier, *Chem. Mater.* **2019**, *31*, 8328.

[23] F. Wu, W. Fitzhugh, L. H. Ye, J. X. Ning, X. Li, *Nat. Commun.* **2018**, *9*, 4037.

[24] G. B. Qu, T. Xia, W. H. Zhou, X. Zhang, H. Y. Zhang, L. G. Hu, J. B. Shi, X. F. Yu, G. B. Jiang, *Chem. Rev.* **2020**, *120*, 2288.

[25] X. L. Fan, L. Chen, X. Ji, T. Deng, S. Y. Hou, J. Chen, J. Zheng, F. Wang, J. J. Jiang, K. Xu, C. S. Wang, *Chem* **2018**, *4*, 174.

[26] Y. Yang, X. Qu, X. Zhang, Y. Liu, J. Hu, J. Chen, M. Gao, H. Pan, *Adv. Mater.* **2020**, *32*, 1908285.

[27] R. M. Qiao, I. T. Lucas, A. Karim, J. Syzdek, X. S. Liu, W. Chen, K. Persson, R. Kostecki, W. L. Yang, *Adv. Mater. Interfaces* **2014**, *1*, 1300115.

[28] P. Olalde-Velasco, J. Jimenez-Mier, J. Denlinger, W. L. Yang, *Phys. Rev. B* **2013**, *87*, 245136.

[29] J. Wang, J. Zhou, Y. F. Hu, T. Regier, *Energy Environ. Sci.* **2013**, *6*, 926.

[30] a) D. A. Shapiro, Y. S. Yu, T. Tyliszczak, J. Cabana, R. Celestre, W. L. Chao, K. Kaznatcheev, A. L. D. Kilcoyne, F. Maia, S. Marchesini, Y. S. Meng, T. Warwick, L. L. Yang, H. A. Padmore, *Nat. Photonics* **2014**, *8*, 765; b) Y. S. Yu, C. Kim, D. A. Shapiro, M. Farmand, D. Qian, T. Tyliszczak, A. L. D. Kilcoyne, R. Celestre, S. Marchesini, J. Joseph, P. Denes, T. Warwick, F. C. Strobridge, C. P. Grey, H. Padmore, Y. S. Meng, R. Kostecki, J. Cabana, *Nano Lett.* **2015**, *15*, 4282.

[31] a) C. S. Wang, Y. S. Meng, K. Xu, *J. Electrochem. Soc.* **2018**, *166*, A5184; b) X. L. Fan, X. Ji, L. Chen, J. Chen, T. Deng, F. D. Han, J. Yue, N. Piao, R. X. Wang, X. Q. Zhou, X. Z. Xiao, L. X. Chen, C. S. Wang, *Nat. Energy* **2019**, *4*, 882.

[32] K. H. Park, D. Y. Oh, Y. E. Choi, Y. J. Nam, L. L. Han, J. Y. Kim, H. L. Xin, F. Lin, S. M. Oh, Y. S. Jung, *Adv. Mater.* **2016**, *28*, 1874.

[33] F. Zhao, Y. Zhao, J. Wang, Q. Sun, K. Adair, S. Zhang, J. Luo, J. Li, W. Li, Y. Sun, X. Li, J. Liang, C. Wang, R. Li, H. Huang, L. Zhang, S. Zhao, S. Lu, X. Sun, *Energy Storage Mater.* **2020**, *33*, 139.

[34] X. F. He, Y. F. Mo, *Phys. Chem. Chem. Phys.* **2015**, *17*, 18035.

[35] S. P. Ong, W. D. Richards, A. Jain, G. Hautier, M. Kocher, S. Cholia, D. Gunter, V. L. Chevrier, K. A. Persson, G. Ceder, *Comp. Mater. Sci.* **2013**, *68*, 314.

[36] a) H. Tang, Z. Deng, Z. Lin, Z. Wang, I.-H. Chu, C. Chen, Z. Zhu, C. Zheng, S. P. Ong, *Chem. Mater.* **2017**, *30*, 163; b) Y. F. Mo, S. P. Ong, G. Ceder, *Chem. Mater.* **2012**, *24*, 15.

[37] Y. Z. Zhu, X. F. He, Y. F. Mo, *ACS Appl. Mater. Interfaces* **2015**, *7*, 23685.

[38] S. Nose, *Prog. Theor. Phys. Suppl.* **1991**, *103*, 1.

[39] X. F. He, Y. Z. Zhu, A. Epstein, Y. F. Mo, *npj Comput. Mater.* **2018**, *4*, 18.

[40] G. Henkelman, H. Jonsson, *J. Chem. Phys.* **2000**, *113*, 9978.